Appl. Phys. B (2013) 113:437–449
DOI 10.1007/s00340-013-5488-0

Applied Physics B
Lasers and Optics

Theoretical treatments of ultrashort pulse laser processing of transparent materials: toward understanding the volume nanograting formation and "quill" writing effect

Nadezhda M. Bulgakova · Vladimir P. Zhukov · Yuri P. Meshcheryakov

Published online: 19 May 2013

Abstract The dynamics of ultrashort-laser-induced generation of free electron plasma inside bulk glass is analyzed. The results of modeling are presented for typical glass modification regimes, obtained on the basis of Maxwell's equations supplemented with the equations describing electron plasma formation and the laser-induced electric current. The model has been demonstrated to allow revealing important features of laser beam propagation in the regimes of dense electron plasma generation such as strong scattering up to complete displacing of light from the plasma region followed by beam refocusing. The geometry of the laser energy absorption zone is determined, and the glass temperature is mapped which may be foreseen at the end of electron–glass matrix relaxation. This, in turn, allows estimating the laser-induced stress levels and making conclusions on the routes of glass modification. Finally, based on the modeling results, the plausible mechanisms are discussed which may be responsible for the formation of volume nanogratings in a number of transparent solids under the action ultrashort laser pulses and laser direct writing anisotropy observed for laser pulses with a tilted front.

N. M. Bulgakova
Optoelectronics Research Center, University of Southampton, SO17 1BJ Southampton, UK

N. M. Bulgakova (✉)
Institute of Thermophysics SB RAS, 1 Lavrentyev Ave., 630090 Novosibirsk, Russia
e-mail: nbul@itp.nsc.ru

V. P. Zhukov
Institute of Computational Technologies SB RAS, 6 Lavrentyev Ave., 630090 Novosibirsk, Russia

V. P. Zhukov
Novosibirsk State Technical University, 20 Karl Marx Ave., 630073 Novosibirsk, Russia

Y. P. Meshcheryakov
Design and Technology Branch of Lavrentyev Institute of Hydrodynamics SB RAS, Tereshkovoi Street 29, 630090 Novosibirsk, Russia

1 Introduction

Since 1996 when it was demonstrated that tightly focused femtosecond laser pulses could induce a local internal increase in the refractive index in bulk transparent glasses [1], the interaction of ultrashort laser pulses with transparent optical materials has attracted a lot of attention as a powerful technique of modification of material properties [2]. This technique is widely adopted in numerous technological applications based on three-dimensional photonic structures in bulk optical materials, such as waveguides [1, 3–7], Bragg gratings [8, 9], Fresnel zone plates [10], beam shapers [11], waveplates based on volume nanogratings (VNG) [12], splitters [13], couplers [14, 15], amplifiers [16], rewritable optical memories [17, 18], and computer-generated holograms [19]. As seen from the above citations, the field of laser writing of optical structures in glasses has been rapidly developing during last 15 years.

While tremendous achievements have been made toward laser-writing techniques and assembling integrated photonic devices, the physical mechanisms underlying glass modifications have not been fully understood. Several models have been developed for studying conditions realized inside transparent matter upon laser excitation in

modification regimes, such as simulations of laser light propagation based on the nonlinear Schrödinger equation [6, 7, 20–22], Maxwell's equations supplemented with the rate equation for free electron generation [23–26], a simplified geometrical model of laser light focusing [27], and analyses of heat-accumulation effects [4, 28]. Only individual attempts are known of considering the whole route of evolution of laser-irradiated matter from its excitation at ultrashort laser pulse timescale through the development of strong temperature gradients, emission of elastic waves, plastic deformations, and heat dissipation, to the final structure imprinted into the transparent matrix [7, 29–31]. However, further development of laser-writing techniques for controllable generation of desired structures in transparent materials is impossible without deep understanding of the governing mechanisms of laser-driven modifications. Apart from the fact that the theory and modeling of the laser-induced processes can be the cost-reducing tools which can allow choosing the optimal conditions and most appropriate materials for particular modifications, they provide a detailed physical understanding of the phenomenon and required material properties for technological applications.

The aim of this paper is to address theoretically a number of extraordinary phenomena observed in glass materials upon laser irradiation, such as volume nanograting formation [10, 18, 32–37] and laser direct writing anisotropy [38]. Although the presented analysis is based on fused silica glass, a similar framework may be applied for other glasses and transparent crystals. A model has been developed to describe ultrashort laser pulse propagation in transparent matter which is based on Maxwell's equations supplemented with the equations describing electron plasma generation and the laser-induced electron current. Based on this model, spatiotemporal dynamics of laser beam propagation has been studied with taking into account self-focusing, free electron generation, and plasma-induced defocusing inside a fused silica sample at particular irradiation regimes employed for laser direct writing. As a result, the geometry of the laser energy absorption zone is determined, and the glass temperature is mapped which may be foreseen at the end of electron–glass matrix relaxation. This, in turn, allows estimating the laser-induced stress levels and making conclusions on the routes of glass modification. Finally, based on the performed studies, the processes are discussed which persuasively explain formation of the VNGs in a number of transparent solids under the action of ultrashort laser pulses and laser direct writing anisotropy observed for laser pulses with the tilted front.

2 Maxwell's model equations

The basics of the model are essentially similar to those reported in [23] with further development by taking into account avalanche ionization and light dispersion. Maxwell's equations for laser beam propagation through a nonlinear absorbing medium can be written in the following form:

$$\frac{1}{c}\frac{\partial \vec{D}}{\partial t} - i\frac{\omega}{c}\vec{D} = -\frac{4\pi}{c}\vec{j} + \mathrm{rot}\vec{H} - \frac{8\pi}{c}W_{\mathrm{PI}}E_g\frac{\vec{E}}{|E^2|}, \quad (1)$$

$$\frac{1}{c}\frac{\partial \vec{H}}{\partial t} - i\frac{\omega}{c}\vec{H} = -\mathrm{rot}\vec{E}. \quad (2)$$

Here the standard denotations are used with E, D, H, ω, j, and c to be electric field, electric displacement field, magnetic field, laser light frequency, electric current, and speed of light, respectively; W_{PI} is the rate of photoionization; E_g is the band gap which is dependent on the field strength. In Eq. (1) it is assumed that the electric field of the beam wave can be presented in the form $\vec{E} = \left(\vec{E}_0 e^{-i\omega t} + \vec{E}_0^* e^{i\omega t}\right)/2$ and for the plane wave the laser field intensity is expressed as:

$$I = \frac{cn}{8\pi}\left|\vec{E}_0^2\right|,$$

where n is the linear index of refraction. Taking into account the energy clamping effect which saturates the laser intensity at a level with the Keldysh parameter $\gamma = \omega\left(m_e^* E_{g0}\right)^{0.5}/(eE_0) > 1$ 1 the multiphoton mechanism of ionization is accepted with the rate $W_{\mathrm{PI}} = \sigma_k I^k (n_{\mathrm{at}} - n_e)/n_{\mathrm{at}}$ reduced by the available ionization centers (n_e and n_{at} are the number densities of free electrons and atoms in undisturbed lattice, respectively; the densities of electrons and holes are considered to be equal; and k is the number of photons needed for exciting a valence electron to the conduction band). For fused silica at 800 nm wavelength, $k = 6$ and $\sigma_6 = 2 \times 10^{-47}$ cm^9/(s W^6) [20]. In simulations here, the atomic but not molecular density of 6.6×10^{22} cm^{-3} is used. For convenience, W_{PI} is rewritten to the form $W_{\mathrm{PI}} = W_{\mathrm{PI0}}\left(|E^2|/E_*^2\right)^k (n_{\mathrm{at}} - n_e)/n_{\mathrm{at}}$. Here $W_{\mathrm{PI0}} = 3.7 \times 10^{34}$ cm^{-3} s^{-1} and $E_*^2 = 8\pi I_*/nc$ with $I_* = 3.5 \times 10^{13}$ W/cm^2 (the laser intensity at which $\gamma = 1$). Then the intensity-dependent band gap width $E_g = \left(E_{g0} + e^2|E^2|/\left(4m_e^*\omega^2\right)\right)$ can be expressed as $E_g = E_{g0}\left(1 + |E^2|/\left(4E_*^2\right)\right)$, where E_{g0} is the band gap in the absence of the electric field (9 eV for fused silica); e is the elementary charge (positive here and everywhere below); ε_0 is the dielectric permittivity of

vacuum; and m_e^* is the reduced electron mass ($m_e^* = 0.64m_e$ according to [20]).

The electric displacement field can be presented as:

$$\vec{D} = \vec{E} + \sum_m \vec{P}_m + \vec{P}_{\rm nl}. \tag{3}$$

The linear part of the media polarization is modeled as a set of oscillators

$$\frac{\partial \vec{P}_m}{\partial t} - i\omega \vec{P}_m = \vec{V}_{Pm}, \tag{4}$$

$$\frac{\partial \vec{V}_{Pm}}{\partial t} - i\omega \vec{V}_{Pm} = -\omega_m^2\left(\vec{P}_m - B_m\vec{E}\right), \tag{5}$$

where $\vec{P}_m$ and $\vec{V}_{Pm}$ are the local material response and its derivative, respectively. For fused silica, $m = 1, 2, 3$; $\omega_1 = 27.539\ \text{fs}^{-1}$; $\omega_2 = 16.21\ \text{fs}^{-1}$; $\omega_3 = 0.19034\ \text{fs}^{-1}$; $B_1 = 0.6962$; $B_2 = 0.4079$; and $B_3 = 0.8975$ [20]. For a particular case of $\vec{E} = \text{const}$, the linear refractive index is expressed as:

$$n^2 = 1 + \sum_m \frac{B_m\omega_m^2}{\omega_m^2 - \omega^2} = 1 + \sum_m \frac{B_m\lambda^2}{\lambda^2 - \lambda_m^2}$$

and, for fused silica at $\lambda = 800$ nm, $n = 1.45$.

In the general case, the nonlinear polarization part of (3) takes into account optical Kerr effect with a term corresponding to the delayed Raman–Kerr optical response ($f_r = 0.18$ for fused silica [6]):

$$\vec{P}_{\rm nl} = \frac{c}{4\pi}n^2 n_2\left((1-f_r)\left|\vec{E}^2\right| + f_r\int_0^\infty R(\tau)\left|\vec{E}^2(t-\tau)\right|d\tau\right)\vec{E},$$

where n_2 is the nonlinear refractive index and the function $R(\tau)$ characterizes the molecular response to the laser light [21]. In this paper in order to decrease the computational costs, our consideration is restricted to relatively small numerical apertures when the contribution of the delayed Raman–Kerr response is small. Hence, in our case

$$\vec{P}_{\rm nl} = \frac{c}{4\pi}n^2 n_2\left|\vec{E}^2\right|\vec{E}. \tag{6}$$

The equations for the density and momentum of free electrons are written as:

$$\frac{\partial n_e}{\partial t} = W_{\rm PI} + W_{\rm av} - \frac{n_e}{\tau_{tr}}, \tag{7}$$

$$\frac{\partial(n_e\vec{\rm v})}{\partial t} - i\omega n_e\vec{\rm v} = -n_e\frac{e}{m_e}\vec{E} - n_e\frac{\vec{\rm v}}{\tau_c}, \tag{8}$$

$$\vec{j} = -n_e e\vec{\rm v}. \tag{9}$$

Here $\vec{\rm v}$ and τ_{tr} are the electron velocity and the characteristic time of electron trapping to the defect states, respectively. For fused silica, the value τ_{tr} accounts for the formation of self-trapped excitons. In the present modeling the value $\tau_{tr} = 150$ fs is used [39, 40]. The electron scattering time τ_c is taken to be 1.27 fs, accounting that the damping factor $\omega\tau_c = 3$ [6, 7]. The avalanche ionization rate is described via the Drude formalism as [6]:

$$W_{\rm av} = \frac{e^2\tau_c n_e\left|\vec{E}^2\right|}{nc\varepsilon_0 m_e E_g\left(1+\omega^2\tau_c^2\right)\left(1+m_e^*/m_e\right)}\frac{n_{\rm at}-n_e}{n_{\rm at}}. \tag{10}$$

In Eq. (10) all the parameters are expressed in SI units. The system of Eqs. (1)–(9) was solved numerically for fused silica irradiated by femtosecond laser pulses in the cylindrically symmetric case, assuming that $\vec{E}^2$ weakly depends on the azimuthal angle φ. The components of the electric field depend on φ as $\mathrm{E}_r = \hat{E}_r(r,z,\mathrm{t})\cos\varphi$; $\mathrm{E}_\phi = \hat{E}_\phi(r,z,\mathrm{t})\sin\varphi$; $\mathrm{E}_z = \hat{E}_z(r,z,\mathrm{t})\cos\varphi$. We control the validity of cylindrical symmetry by ensuring the condition $||\hat{E}_r^2| + |\hat{E}_z^2| - |\hat{E}_\phi^2|| << |\hat{E}_r^2| + |\hat{E}_z^2| + |\hat{E}_\phi^2|$. The incoming laser beam at the sample surface ($z = 0$) corresponds to the linear polarized light:

$$\hat{E}_r(r,0,t) = E_{\rm in}\exp\left(-r^2/w^2 - t^2/\tau_{\rm L}^2 - ik_0r^2/(2f)\right),\quad \hat{E}_r = -\hat{E}_\phi. \tag{11}$$

Accordingly, $E_y = 0$; $E_x = \hat{E}_r$. Here $E_{\rm in} = [16\varepsilon_{\rm L}/\left(ncw^2\tau_{\rm L}\sqrt{\pi/2}\right)]^{1/2}$, where $\varepsilon_{\rm L}$ and $\tau_{\rm L}$ are the pulse energy and duration, respectively; $w = w_f\left(1 + d^2/z_f^2\right)^{1/2}$ is the beam radius at the distance d from the geometric focus; w_f is the beam waist; $z_f = k_0 w_f^2/2$ is the Rayleigh length; $k_0 = n\omega/\mathrm{c}$; $f = d + z_f^2/d$ is the beam curvature.

At the other boundaries, the zero boundary conditions lead to the reflected waves and the necessity of using a large computational region (r_0, z_0). To avoid this, the conditions of the zero Riemann invariants on the incoming characteristics are applied:

$$nE_r - B_\varphi = 0;\ nE_\varphi + B_r = 0 \quad \text{at} \quad z = z_0;$$

$$nE_\varphi - B_z = 0;\ nE_z + B_\varphi = 0 \quad \text{at} \quad r = r_0.$$

It must be noted that in Eqs. (7)–(8) the terms of the $\mathrm{div}(\vec{\rm v}n_e)$ and $\partial\left(n_e v_i v_j\right)/\partial x_j$ kinds and the term involving the Lorentz force have been disregarded. The contributions of the convective terms for the typical irradiation regimes of material modification were studied, and the plasma density change due to these terms was found to be only approximately 10^{-4} as compared to the results with disregarding such terms. Hence, these terms may be omitted in order to considerably reduce computational costs. As for the Lorentz force, its contribution to the

electron current (Eq. 8) is smaller by factor of v/c as compared to the electric field force, and thus, it may also be safely neglected for the clamped laser intensity inside transparent solids.

The results of simulations presented below are characteristic of the two modification regimes of fused silica, of a relatively low-energy pulse (LEP) when nanograting structures are obtained at multipulse irradiation ($\varepsilon_L = 1$ μJ, 150-fs pulse duration [32]), and of a higher-energy pulse (HEP) above which one may expect the transition to a strong modification [6] resulted from material melting that may involve creation of void-like structures by single laser pulses ($\varepsilon_L = 2.5$ μJ, 80 fs). Note that the power of both pulses studied is well above the self-focusing regime (2.8 MW for fused silica [21]).

A comment should be made on the effect of focusing conditions found in simulations. Here the simulations are limited to the beam waist of 1 μm. Attempts to decrease beam waist lead to violation of the cylindrical symmetry caused by the electron current and, additionally, to the energy nonconservation in the simulation process. For the regimes with NA > 0.35, the problem becomes essentially three-dimensional. The realization of a 3D code for describing laser-induced plasma generation inside transparent solids which requires extremely large computational resources is now under development.

3 Spatiotemporal dynamics of plasma formation and laser beam propagation

Snapshots from the calculations (Fig. 1) show how the free electron plasma is developing during the laser pulse propagation through the focal zone. In the figure the distribution maps of the free electron density are compared for two pulses whose energy differs by 2.5 times. The more energetic pulse is of shorter duration so its peak intensity in vacuum is approximately 4.6 times higher as compared to the lower-energy pulse. The geometric focus is marked by the white dashed lines while the location of the laser pulse maximum is indicated by the black dots on the z-axis. Several important aspects can be noticed. In the LEP regime (Fig. 1a), ionization starts before the geometric focus (410 fs) and is evidently induced by the

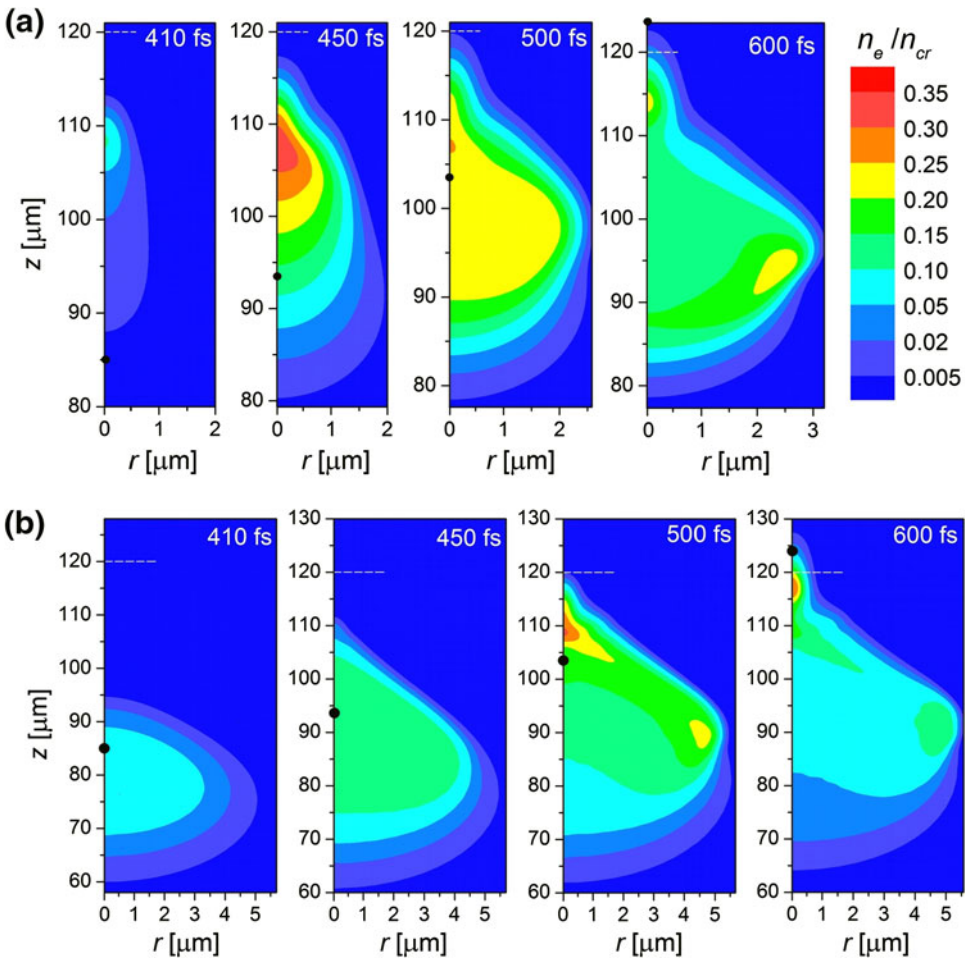

Fig. 1 Dynamics of the free electron density in fused silica for $\varepsilon_L = 1$ μJ, $\tau_L = 150$ fs (**a**) and $\varepsilon_L = 2.5$ μJ, $\tau_L = 80$ fs (**b**). The laser beam propagates from the *bottom*. The electron density is normalized by the critical electron density, $n_{cr} = \varepsilon_0 m_e \omega^2/e^2$, whose value is 1.74×10^{21} cm^{-3} for the laser wavelength of 800 nm. Geometric focus of the beam (marked by *dashed lines*) is located at the distance $z = 120$ μm from the sample surface. Calculations are started at a negative time moment to ensure that the intensity of the beam front cannot induce any excitation at the initial time moments. At the time moment $t = 0$, the maximum of the beam is at z = 0 (sample surface) and its location upon beam propagation is marked by the *black dots*

very front of the laser pulse. In the HEP case (Fig. 1b) at the same time moment, the ionized region is located much farther from the focus. This difference is explained by the fact that in the HEP regime the ionization threshold of the laser intensity is reached earlier relative to the geometric focus as compared to the LEP case. As a result, the pulse front is considerably depleted of energy in the ionization region and, thus, cannot induce ionization closer to the focus as can be seen in Fig. 2. One can notice that at the early stages of the LEP propagation, the electron plasma is developing rather in the direction toward the laser, whereas in the HEP regime the ionization front moves forward with the laser beam. Interesting is that the maximum levels of the plasma density in the two regimes are essentially the same and remain considerably subcritical. However, in the LEP case the density of the developed electron plasma at $t \geq 500$ fs is almost quasi-uniform within the excited region, whereas in the HEP case ionization is more localized and the signs for double focusing can be noticed. Indeed, comparing electron density snapshots at 500 and 600 fs in Fig. 1b, one can recognize a second maximum which arises and shifts along the beam axis closer to the geometrical focus. The listed aspects are important for explaining the mechanism of the periodic structure formation (Sect. 4). In the further evolution, the more energetic pulse penetrates deeper to the focal zone (not shown here). Plasma decays quite slowly, and as the simulations show, in three hundred femtoseconds after its maximum, it still stays at a level of one-third of the maximum value.

Figure 2 presents snapshots of the laser intensity upon beam propagation toward the geometric focus. Interesting is that for the LEP regime the snapshots resemble the hydrodynamic picture of flow over the blunt body where a plasma "body" generated by the beam front completely displaces the rest of the beam from the plasma region (Fig. 2a). The situation is even more dramatic for the HEP regime where *strong plasma scattering* completely displaces the beam to its periphery from where it is again experiencing self-focusing behind the plasma region (Fig. 2b). Beam self-focusing after strong defocusing (scattering) by the electron plasma is conditioned by the fact that, according to the simulation results, though the laser energy absorbed in the sample during the beam propagation can integrally reach several dozens of percentage depending of the beam energy, the beam power stays above the self-focusing regime. Figure 2 clearly demonstrates the intensity clamping effect when for the beams with considerably different power, the maximum intensity levels differ insignificantly and safely fall to the

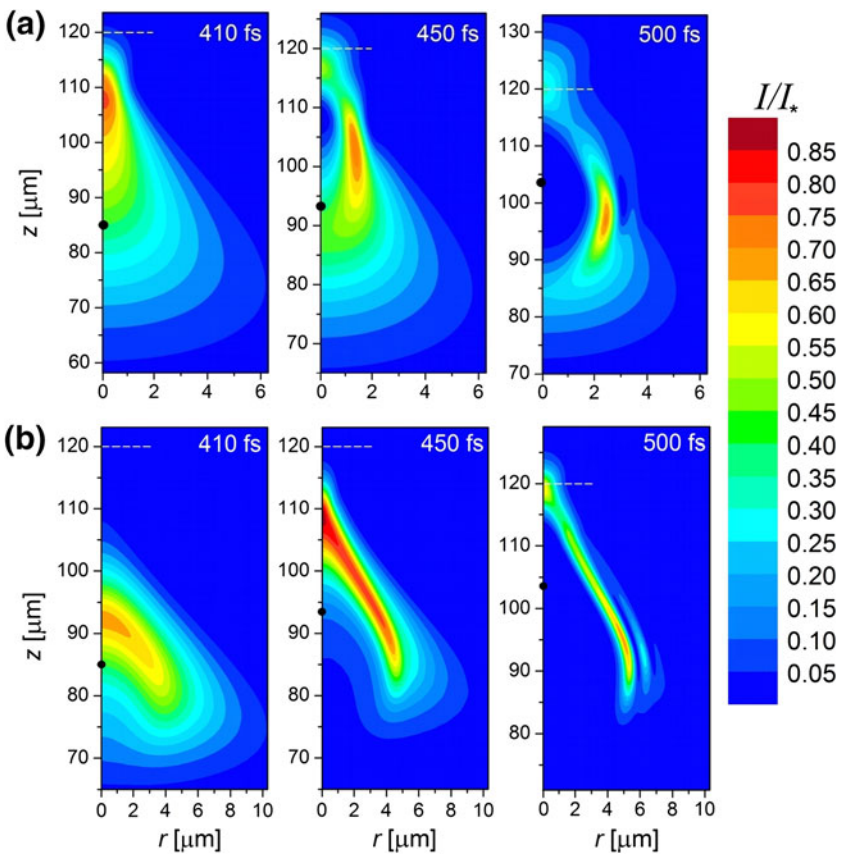

Fig. 2 Instantaneous maps of the laser beam intensity for the conditions of Fig. 1. **a** $\varepsilon_L = 1$ μJ, $\tau_L = 150$ fs; **b** $\varepsilon_L = 2.5$ μJ, $\tau_L = 80$ fs. The intensity is normalized by the value I_* at which the Keldysh parameter $\gamma = 1$ ($I_* = 3.5 \times 10^{13}$ W/cm^2)

regimes of *multiphoton ionization*, thus supporting the results of simplified modeling [27].

The absorbed laser energy distribution integrated over the simulation time can be converted to the lattice temperature map, assuming that, at picosecond timescale, all the locally absorbed energy is spent solely for the lattice heating after electron-lattice thermalization and electron recombination. This assumption is reasonable in view of low heat conductivity of dielectric materials. Applying the thermoelastoplastic model [7, 41], the instantaneous distributions of the material stress can be obtained. The lattice temperature and stress maps are presented in Fig. 3a, b, respectively, for the two cases studied. In the LEP case the matter stays below the melting point. Although the transient stress level exceeds the static tensile strength of 48.3 MPa tabulated for fused silica at the normal conditions, upon dynamic loads materials withstand stress levels much higher than the static ones. Hence, creation of a bubble or void cannot be expected in this case. The induced high stress gradients of order of (60–70) MPa/μm (Fig. 3b) will result in formation of a strong compression wave, propagating from the heat-affected zone toward virgin material, which will lead to rarefaction of the regions of the enhanced temperature and creation of a densified envelope surrounding expanded core [6, 7]. It should be noted that if matter is heated above the melting point, its strength drops by several orders of magnitude. Hence, it may be expected that our HEP regime (see Fig. 3, right) falls to a boundary above which bubble/void formation may be observed (see, e.g., [6, 42]). Also, it must be underlined that for bubble/void formation, it is far not obligatory to reach or exceed stress levels of Young's modulus though such stress levels may be attainable by beam focusing with high numerical apertures (NA > 1), resulting in creation of warm dense matter conditions [43].

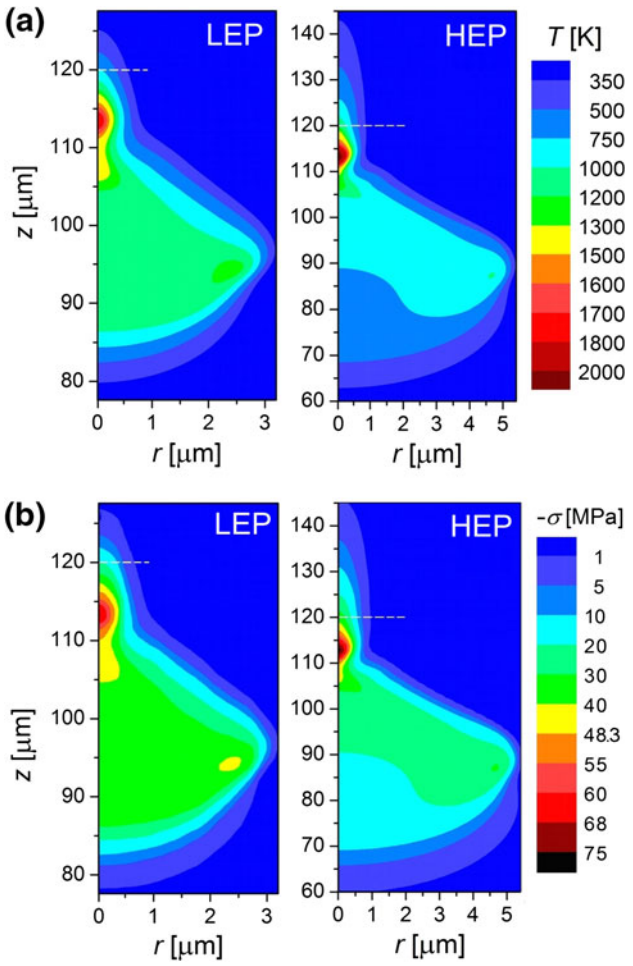

Fig. 3 The *maps* of the temperature (**a**) and thermal stress (**b**) immediately after electron-lattice thermalization in the LEP (left) and HEP (right) regimes. The stress level of 48.3 MPa is the tensile strength value tabulated for fused silica. Note that the stress sign is negative

At the first glance, it looks surprising that the maximum electron density is somewhat higher in the LEP case while the higher temperature is achieved in the HEP case. However, the absorbed energy includes the kinetic energy of electrons. The higher laser intensity at the near-focal region for the HEP case (Fig. 2, 450 and 500 fs) results in a larger velocity of electrons and, hence, in larger absorption, in accordance with Eq. (1).

It must be mentioned that anomalous compaction of fused silica glass upon heating and melting may affect laser modification process [44]. However, there is no yet complete understanding of how glass compaction/rarefaction proceeds at extremely fast timescales of ultrashort excitation. Kinetics of rearrangement of glass bonds may strongly lag behind heating up and cooling. Upon ultrafast heating on ps timescale with realization of high pressure (high negative stress), a compressive wave is formed propagating from the high temperature zone and the latter may occur under a negative pressure (tensile stress) at timescales below 10 ns [7]. The appearance of rarefaction region upon glass modification [6] indicates that dynamic behavior of matter under fast local temperature/pressure loads with producing material deformation is more important than simple thermal expansion. Note that "fast" heating and cooling in [44] imply seconds while all the picture of heating/cooling under ultrafast laser excitation terminates at microsecond timescale with heating during 1–10 ps.

4 On the theory of volume nanograting formation

Based on the above modeling of the two irradiation regimes, some important conclusions can be made on the origin of the ultrashort-laser-induced VNGs discovered in a number of transparent oxide materials [32, 33, 35]. After

discovery in 2003 [32], the VNGs, in particular in fused silica, have become an exciting object for research [see, e.g., 18, 33–37, 45] and an important element for a variety of existing and promising applications in optics and photonics [45]. In spite of extensive fundamental research on this amazing phenomenon with increasing areas of applications, VNG formation under the action of ultrashort laser radiation remains a mystery.

The origin of the VNGs is attributed to interference of plasma waves with laser light [32], formation of nanoplasmas followed by self-organization into nanoplanes through memory effects [18, 34], and interference of two modes of ultrashort-living exciton–polaritons [46]. Explaining VNG formation by light interference with the main mode of plasma oscillations requires the near-critical electron density and free electron energies of hundreds or even thousands of eV [32, 33]. Such free electron parameters would lead to creation of multiply charged ions with complete breaking of bonds inside the excited area, followed by hydrodynamics similar to that described in [29, 43]. The Tonk-Dattner resonances in confined plasmas [47–49] may be an alternative to the main plasma mode, implying reasonable electron energies of order of 10 eV. However, according to the estimation based on the dispersion relation [47]

$$\omega_m^2 = \omega_p^2 + (3kT/m_e)k_m^2, \quad m = 1, 2, 3, \ldots$$

accounting the actual electron density profiles (Fig. 1), the observed VNG periods can be described by a high-order m of the resonance frequency (in the range of 100–1,000). Presumably, the conditions for the low-order Tonk-Dattner resonances may be realized in near-surface plasmas upon excitation of band gap materials where the critical and supercritical electron density may be easily achieved [50] and surface ripples are formed through surface diffusion and ablation. In-volume plasmas under such conditions ($n_e \approx n_{cr}$, $T_e = 5$–10 eV) will lead to lattice superheating toward high temperatures and stresses incompatible with gentle formation of the VNG structures.

Another argument against the plasma wave mechanism of VNG formation is demonstrated in Fig. 4. The figure presents a snapshot of the value of $(n_e–n_i)/n_e$ across the laser-excited region obtained in simulations of a model problem on electron plasma dynamics for the case of $\varepsilon_L = 1$ μJ, $\tau_L = 150$ fs, taking into account the terms $\mathrm{div}(\vec{\nabla} n_e)$ and $\partial(n_e v_i v_j)/\partial x_j$ in order to describe collective electron oscillations in a more precise manner. The electron plasma cross section corresponds to the conditions shown in Fig. 1a (500 fs, $z \approx 110$ μm). The maximum of deviation of the electron density from the ion one is only ~0.01 % at maximum $n_e \sim 5 \times 10^{20}$ cm^{-3}. The analysis based on the dispersion relation shows that plasma

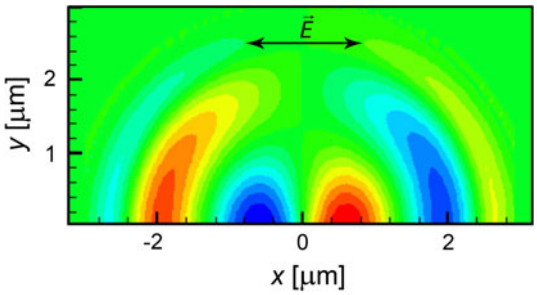

Fig. 4 Snapshot of the $(n_e–n_i)/n_e$ value across the laser-excited region obtained in simulations of a model problem on electron plasma dynamics for the case corresponding to $\varepsilon_L = 1$ μJ, $\tau_L = 150$ fs. For further details see the text

oscillations decay quickly after the laser pulse termination with a characteristic time of plasma wave traveling across the laser-excited region (only several dozens of fs). It is evident that there is no tendency of plasma oscillations to form straight parallel structures within the laser-excited region. Furthermore, due to nonuniformity in the electron density and energy profiles, period and amplitude of oscillations are changing across the excited zone as also was observed for the Tonk-Dattner resonances (see, e.g., Fig. 9 in [47]).

Recently proposed mechanism of exciton–polariton interaction may be important at low densities of low-energy free electrons which rapidly transform into excitons after excitation to the conduction band [51]. At $n_e \geq 10^{19}$ cm^{-3}, the exciton–polariton interaction should be heavily screened by the electron plasma when it begins to efficiently absorb laser energy and to develop secondary electrons. Note that for laser pulses of several hundreds of fs, avalanche ionization becomes dominant [52, 53], while for the few-cycle pulses whose temporal length is smaller or comparable with the electron collision time, collisional ionization can presumably be avoided almost completely [54]. The nanoplasma mechanism of nanograting formation may be initiated between the two extremes, plasma wave interference with laser light and exciton–polariton interaction, with evolution toward the critical density at nanoplane sites [18, 34]. Understanding of the actual mechanisms of VNG formation may open new ways for controllable fabrication of sub-wavelength nanostructures (nanogratings) in a number of transparent materials which are already utilized in optical technologies [12, 45].

The regimes of near-IR ultrafast laser formation of the VNGs in fused silica glass lie, for pulse durations of 50–500 fs, in the range of laser pulse energy from ~0.1 μJ to more than 1 μJ [18]. For laser pulses shorter than 150 fs, the threshold energy for VNG formation is somewhat higher, while at $\tau_L > 150$ fs the VNG structure becomes coarse with increasing pulse energy above 300 nJ [18]. The mentioned regimes are typical also for waveguide writing

and characterized by a peculiar modification zone where, in addition to glass compaction regions, on-axis confined volumes with reduced refractive index are formed already by single-pulse action, clearly indicating material expansion (see, e.g., Fig. 5 in [6] and Fig. 3 in [36]). The latter points to noticeable heating and relocation of matter within the focal volume that, in its turn, implies a relatively high level of excitation of electron plasma. The excitation level may be understood by considering the laser energy balance. Once the energy absorbed due to electronic excitation is stored in a localized volume of the sample in view of slow heat conduction, the level of heating of the material matrix on ps timescale can be evaluated, assuming the definite levels of the density of free electrons and their average energy. Then the energy balance may be written in the form:

$$c_p\rho(T^* - T_0) = n_e e\left(E_e + E_g\right) \quad (12)$$

where T^*, T_0, and E_e are the lattice temperature directly after electron-lattice thermalization, the initial lattice temperature, and the average energy of free electrons upon laser excitation, respectively; c_p is the lattice heat capacity; ρ is the material density (note that in (12) E_e and E_g are in eV). Expression (12) implies that all the energy from the electronic subsystem including the band gap energy is transmitted to the lattice. Although free electrons are first trapped to the self-trapped exciton (STE) states, the STE population decays at subnanosecond time after excitation [40] and only a small fraction on the STEs (approximately 10^{-3}) turns to the defect states such as E'-centers [55]. Thus, the energy accumulated in the defect states after single-pulse excitation may be disregarded in evaluating the energy balance. From (12) one can extract the pairs of the free electron energy and density which secure material heating to a threshold temperature T^*, for example, annealing, softening, melting, and sublimation.

According to a number of studies [56–58], typical values of free electron energy in wide-band gap dielectrics are in the range of 5–15 eV. This is explainable from the viewpoint of ionization kinetics. Free electrons absorbing photons may produce secondary electrons by collisional ionization if their energy exceeds the material band gap. This sets limits on the average electron energy to approximately 1.5 E_g at relatively long pulse durations (at least $\geq$100 fs) when free electrons have time to gain enough energy from the beam by inverse bremsstrahlung absorption for developing the avalanche process. The electron number density is much more debated. The pump-probe experiments report on maximum electron densities of 5×10^{19} cm^{-3} or even smaller (see, e.g., [59]) while the simulation results obtained in the frames of different models for laser wavelength of 800 nm ($n_{cr} = 1.74 \times 10^{21}$ cm^{-3}) give values in the range $\sim$(0.1–0.5) n_{cr} [6, 7, 20, 21, 23, 27].

It should be underlined that experimental data on n_e are the evaluations, based on the Drude model, from the measured values of the transient change of refractive index. These estimations contain at least several poorly known parameters. In the evaluation procedure, it is assumed that the electron density is uniform along the probe beam path through the laser-excited region and immediately drops in the region boundaries. This is far from the actual situation as the electron plasma is essentially nonuniform (see Fig. 1). Another parameter is the effective free-carrier mass which, according to different studies, may differ up to 4 times for fused silica [20, 60]. This variable value is dependent on the electron energy and, hence, on the irradiation conditions [61]. Most dramatic effect may be due to the electron collision time whose reported values vary in the range of 0.2 fs [62] to 23.3 fs [63]. Taking into account all these parameters, the error of such estimations may be more than an order of magnitude. On the other hand, to induce irreversible material expansion in the excited region with a single laser pulse at 800 nm wavelength [6], the silica glass transition point (1,261 K [64]) must be exceeded that, according to Eq. (12), implies excitation up to 0.3 n_{cr} integrally over the pulse with the average free electron energy of $\sim$10 eV (note that the maximum electron density may be lower in view of extremely fast electron trapping time followed by the re-excitation process). Namely, such order of the characteristic electron plasma parameters has been obtained in numerous modeling attempts [6, 7, 20, 21, 23, 27], including the present study. Our further consideration is based on these characteristic plasma parameters and on the spatiotemporal evolution of the plasma density and the beam intensity (Figs. 1, 2).

Recently, Hörstmann-Jungemann et al. [35] have demonstrated that, upon translating the laser beam focus from the bulk toward the sample surface, the VNG structures written in sapphire transfer to laser-induced periodic surface structures (LIPSS) without essential change in the periodicity. Some changing in the period may be attributed to larger laser intensity in view of the absence of the clamping effect upon surface irradiation. This is indicative of a unified mechanism which is responsible for both the VNGs and LIPSS formation as proposed in [35]. The LIPSS formation mechanism is described in the frames of a surface-scattered wave model [65] as a "radiation remnant" emerging from polarization of a rough surface ("selvedge") which behaves as a "dipole sheet." The material beneath this layer sees the effective electromagnetic field which is a superposition of the incident wave and the waves created by "dipole sources" on the surface. The superimposed field structure results in inhomogeneous deposition of laser energy and formation of the rippled patterns. This is described in terms of the efficacy factor η which characterizes the efficacy at which laser light

coupling with the surface roughness results in inhomogeneous laser energy absorption $A\left(\vec{k}\right)$ with $\vec{k} = \left(k_x, k_y\right)$ to be the vector of the induced periodic structure [65–67]:

$$A(\vec{k}) \propto \eta\left(\vec{k}, \vec{k}_i\right) b\left(\vec{k}\right). \tag{13}$$

Here $\vec{k}_i$ is the component of the laser wave vector parallel to the selvedge dipole sheet, and $b\left(\vec{k}\right)$ is the Fourier component of the roughness. The efficacy factor may be derived analytically under the assumptions that (1) the selvedge thickness is much smaller as compared to the laser wavelength and (2) the selvage thickness is small compared to the periodicity of the absorption profile.

An important question arises on what can play a role of "selvedge" for volumetric laser energy absorption into the periodic pattern of the VNG. The "forest fire" model of laser-induced breakdown of dielectrics [68] resulted in nanoplasma formation [18, 34] may be a key element in explaining the intriguing phenomenon of VNG. As hypothesized in [18, 34], upon repeated irradiation, nanoplasma sites evolve into nanoplanes. However, the evolution mechanism into nanoplanes of certain periodicity is unclear. On the other hand, the nanoplasma volumes behave as dipoles in the electromagnetic field of the laser pulse, and hence, the irradiation zone becomes polarized with dipole–dipole interaction of the nanoplasma islands. From this viewpoint, the VNGs may be considered as the "radiation remnants" emerging from polarization of a "rough" volume similar to a rough surface at LIPSS formation.

For the volumetric case of laser energy coupling with a coarse polarized matter, the efficacy factor theory becomes extremely complicated and may not be resolved analytically. A way to get more insight to the VNG formation can be based on the FDTD modeling that was recently realized for LIPSS [69]. Although at present such simulations would be unreasonably computer-time-consuming with only a qualitative picture in view of impossibility to model the whole laser-excited volume, this approach looks to be most reliable and hopefully will be possible in future. At the present stage, some important qualitative conclusions toward understanding the VNG formation may be made and such an attempt is presented here, in particular on the VNG periodicity.

For band gap materials, the theory of LIPSS formation developed by Bonse et al. [66] combines the generally accepted first-principles theory by Sipe et al. [65] with the Drude model describing dynamics of optical material properties upon laser excitation of electron plasma. The improved theory [66] describes well low-spatial-frequency LIPSS with a characteristic period $\Lambda \sim \lambda$ or λ/n while it cannot explain appearance of high-spatial-frequency LIPSS (HSFL) with $\Lambda = 200$–280 nm which are evidently more related to the VNGs. The HSFLs are well described by introducing the second harmonics generation (SHG) into the classical Sipe's theory supplemented with the Drude model [67] which yields $\Lambda \sim \lambda/(2n)$. Moreover, it has been shown [67] that the SHG is efficiently generated under the HSFL formation conditions. The SHG is known to accompany interaction of ultrashort laser pulses with underdense and critical-density plasmas with strong concentration gradients where inhomogeneity space scales are of order or smaller as compared to the irradiation wavelength [70, 71]. Under the typical conditions of VNG formation, the spatial scales of laser-generated plasmas are of few micrometers [18, 32–37] that implies large density gradients at the plasma boundaries and possibility of the SHG. The simulation results reported in this work and elsewhere [6, 7, 20, 21, 23] also show existence of strong electron density inhomogeneities within the laser-excited zone with subwavelength spatial scales. Hence, harmonics generation may be a key factor governing the VNG spatial period. Note that the third harmonics can be generated even more efficiently than the second one, especially at relatively low laser pulse energies because of lower electron density gradients, that can explain reduction in the grating period toward 100-nm scale with decreasing laser pulse energy [32, 33]. It was demonstrated that by adding the second harmonics (SH) to the fundamental one upon multipulse irradiation of ZnSe surface, it is possible to efficiently control the orientation and quality of LIPSS by rotating SH polarization [72]. Furthermore, SH admixture improves the quality of LIPSS while the latter are not formed with only SH light. Similar experiments can also be performed for the conditions of the VNG formation that would demonstrate the actual SHG role in creating periodic structures inside transparent materials.

As shown in [32, 33], the VNG periodicity is increasing with the beam energy and decreasing with number of pulses at the same energy. For in-volume multipulse irradiation of transparent materials, change of refractive index Δn may substantially add to variation in periodic structure spacing. It involves contributions from accumulation of defects (Δn_{trap}) [39, 73], heat (Δn_{th}) [73, 74], and stress (Δn_P) [74] as well as density change (Δn_ρ) [73, 75], in addition to electron plasma (Δn_{Drude}) and the Kerr effect (Δn_{Kerr}) contributions upon laser action [66, 73]:

$$\Delta n = \Delta n_{\text{trap}} + \Delta n_{th} + \Delta n_P + \Delta n_{\text{Drude}} + \Delta n_{\text{Kerr}} + \Delta n_\rho. \tag{14}$$

Although the thermal and density effects are interrelated, here they are intentionally separated as at high-repetition multipulse irradiation the material may be out of temperature–density equilibration of its structure. The terms in the right-hand side of (14) are dynamically

changing from pulse to pulse and contribute with different signs to the total change of refractive index that makes predicting of the VNG period extremely cumbersome and rather speculative. More understandable is the appearance of the second periodicity, along the laser beam axis which has λ/n in the VNG head and increasing toward its tail. The question on this periodicity seems to be resolved within the frames of the exciton–polariton interaction model [46] where the z-component of the laser electric field was shown to result in the mentioned nanograting modulation along the beam axis. It can be thought that the model [46], which is based on dipole–dipole interaction of excitons–polaritons, may seemingly be applied for describing dipole–dipole interaction of nanoplasmas [18, 34] as a simplifying predictive instrument, alternative to the FDTD simulations which are extremely time- and resource-consuming.

A comment should be made on the possibility of important contribution of ionization instability in the formation of the VNGs. The periodic absorption of laser energy, as is implied by the Sipe's theory, is a highly nonlinear effect for wide-band gap dielectrics. According to the "forest fire" model [68], an ionization event leads to strengthening the electric field around the ionized atom that results in a higher probability of ionization in the nearest vicinity. This mechanism is responsible for nanoplasma formation [18, 34]. It has been predicted by simulations for a gas plasma [76] that a scattered wave, even if being very weak (less than 1 % of pump wave amplitude), may induce strong ionization-induced scattering instability with a fine periodic structure of ionization pattern. The mechanism of this instability is also referred to strengthening the electric field of the laser wave when, at definite perturbations of plasma and laser wave parameters, ionization starts to develop uncontrollably. The ionization instability may be described in the frames of the dispersion relation [76] which, for some specific cases, yields the instability criterion:

$$n_{\mathrm{at}}/n_{cr} > (16\omega/\alpha W_0)/\left(\omega^2 L^2/c^2\right). \quad (15)$$

For fused silica and with a typical transversal size of the laser-induced electron plasma ($L \sim 4$ μm) and $W_0 = 9.6 \times 10^{-70} I^6$ s^{-1} [20], the critical values of laser intensity for the development of the stimulated ionization scattering instability can be evaluated as $I_{\mathrm{ins}} \sim 2 \times 10^{13}$ W/cm^2 or $\sim 0.6 I^*$ that is attainable under the irradiation conditions studied here (Fig. 2). Note that the contribution of avalanche ionization may further reduce the I_{ins} value that, however, depends on the electron density and pulse duration. Hence, for fused silica the ionization instability may be verified experimentally by applying a weak perturbation wave at different angles to the pump laser beam [76]. The ionization instability development may be responsible for extremely thin width of nanoplanes forming the VNG structures. Important is that the development of the mentioned instability does not require the electron densities close to the critical one but instead assumes a precipitous ionization dynamics [76]. According to [76], this instability occurring at a transient stage of the ionizing pulse results in plasma inhomogeneities or *ionization strata* whose spatial period must be dependent on scattering and plasmon polariton dynamics [65–67]. A natural consequence of the *strata* structure development is a feedback loop that appears as enhanced absorption of the light in the strata maxima, higher heating, and higher concentration of defect states in the strata maxima sites leading again to higher absorption.

Two important questions are still present. (1) Why are the VNGs formed only in a number of materials while the mechanism has to be unified for many transparent materials whose properties satisfy Eq. (15) at definite irradiation conditions? (2) Why does the VNG formation require multipulse irradiation regimes? To answer these questions, we notice that contrary to the LIPSS structures which are formed on the surfaces of almost any materials [65–67], the VNGs have been observed only inside several oxides, namely fused silica, Al_2O_3, and TeO_2 [32–34]. These oxides are characterized by different coordination numbers of oxygen compared to a metallic/semiconductor/metalloid constituent. Additionally, the VNGs are not observed in the composite glasses having alkali metal additions. It is evident that as upon the VNG formation the material does not have an additional degree of freedom of surface diffusion/ablation inherent for the LIPSS structures, the VNG formation may only be governed by internal chemical restructuring or latent cracking. Therefore, the chemical composition is a key element responsible for ionization strata imprinting to the material matrix. For this, the material matrix must be "softened" in the particular zones of ionization maxima through bond-breaking and defect accumulation. It may be conjectured that the nonmetallic elements, if being less bound into the matrix as compared to metallic/semiconductor/metalloid constituents, can be released and, presumably, form stable gas molecules already at the stage of multipulse laser exposure. In the case of fused silica, only small amount of excited electrons are turned finally to the defect states [55] and, hence, many pulses are required to achieve sufficient stratified softening of the material for imprinting the ionization scattering instability into the material matrix. Important is that in alkali-metal-containing glasses, alkali atoms are not directly embedded into the glass matrix and the latter contains abundant nonbridging oxygen (NBO) sites. Both alkali metal atoms and NBO sites are primarily ionized without a noticeable damage of the matrix, thus preventing stratified accumulation of the matrix defects. In the

materials with equal coordination numbers for metallic/semiconductor/metalloid and nonmetal atoms, one may hardly expect preferential release of one of the components from the matrix.

The VNG imprinting process may be schematically imagined as presented in Fig. 5. Multipulse irradiation of certain materials leads to gradual expansion of the excitation carrot-like region surrounded by a rigid densified envelop and stratified accumulation of the defect states. Cross section of this region is shown in Fig. 5, left. During laser exposure, from pulse to pulse the defects may be healed due to their preferential excitation and accumulate in the other sites, which explains dependence of the VNG period on the number of pulses [32]. The heat conduction calculations show that even at relatively low repetition rates of 100 kHz or below, the excited zone inside the glass cannot be cooled down to the initial temperature so that its temperature is enhanced till the laser pulse termination. Hence, it may be concluded that the final imprinting of the VNGs presumably occurs after laser exposure termination when the matter in the excited zone tends to compact while the rigid envelop prevents material inflow into the zone of reduced density. As a result, the matter fails in "weak" sites of defect accumulation, resulting in formation of nanopores [77] (Fig. 5, right) or even nanocracks [33, 34] that resembles cracking the desert ground with, however, more directed cracking due to specific stratified "ground" softening.

Finally, at least two conditions favoring VNG imprinting into material matrix can be listed:

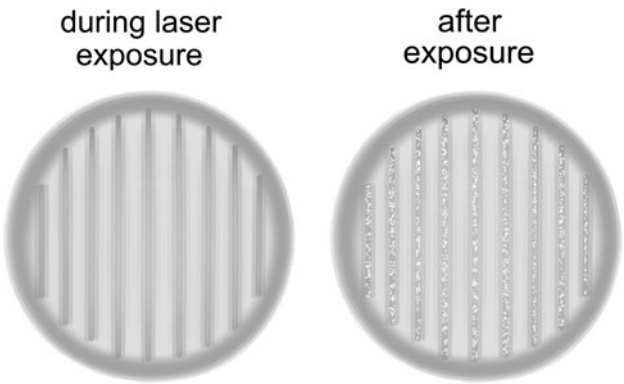

Fig. 5 Schematics of the laser-affected zone of fused silica glass in the regimes of VNG formation. The laser light hits the target perpendicularly to the figure plane. Polarization vector is directed horizontally. The characteristic radius of the modified zone is ~1 μm. *During laser exposure*, the laser-excited region is expanding with creation of an envelope of densified matter (*dark gray ring*) and the strata of the accumulated defect states (*vertical stripes*) are formed perpendicular to polarization (left). *After exposure*, upon cooling, the matter in the excited zone tends to compact while a rigid envelop keeps its shape. As a result, the matter fails along its weak sites of the accumulated defects with appearance of porosity or even cracks

- A transparent solid should be free of alkali metal constituents;
- The coordination number of different constituents must be different to ensure the nonmetallic element to be released from matrix and, presumably, to form stable gas molecules (e.g., O_2 and probably F_2 for fluorides with rutile structure).

Although much research, both experimental and theoretical, must be performed for getting further insight into the fascinating phenomenon of VNG formation, we believe that the performed analysis adds to understanding the VNG effect and may link the VNGs with the LIPSS. It should also be mentioned that the role of the glass chemistry might be more complex due to preexisting defects and impurities [77, 78].

5 On the origin of laser-induced anisotropy upon laser writing in glass materials

The performed modeling gives us another possibility to propose a mechanism that may explain the observed anisotropy of laser direct writing (the "quill" writing effect) in glasses attributed to the laser pulse front tilt (PFT) [38]. It is shown that the plasma is excited by the very front of the laser pulse (Fig. 1) and the rest of the pulse is mostly scattered by the formed plasma. In such situation, even a small PFT will produce free electron plasma with maximum density slightly shifted with respect to the beam axis as schematically shown in Fig. 6. Asymmetric scattering of the rest of the laser pulse by the PFT-produced electron plasma will further increase asymmetry, resulting in the more defect states created off-axis that is important for excitation by the next laser pulses. As a result, even slight asymmetric beam scattering may induce writing anisotropy by the following way.

If laser beam scanning is directed toward the density maximum created by the previous laser pulses (Fig. 7a), plasma generation by the next pulses starts well before the geometric focus due to the accumulated defect states from the previous pulses. This leads to the beam energy depletion due to both energy expenditure for electron excitation and plasma scattering of the rest laser beam, thus resulting in reduced energy penetration to the focal region and, hence, in a "soft" modification as a whole. This can be considered as a pretreatment of the material by the previous pulses. If the beam is moved in the opposite direction, to the "less pretreated" material sites, the beam penetrates deeper to the focal region, resulting in more energy absorption there and, hence, in stronger modification (Fig. 7b).

To corroborate the proposed mechanism of "quill" writing, a 3D modeling is required which is extremely time- and labor-consuming and requires unreasonable computer

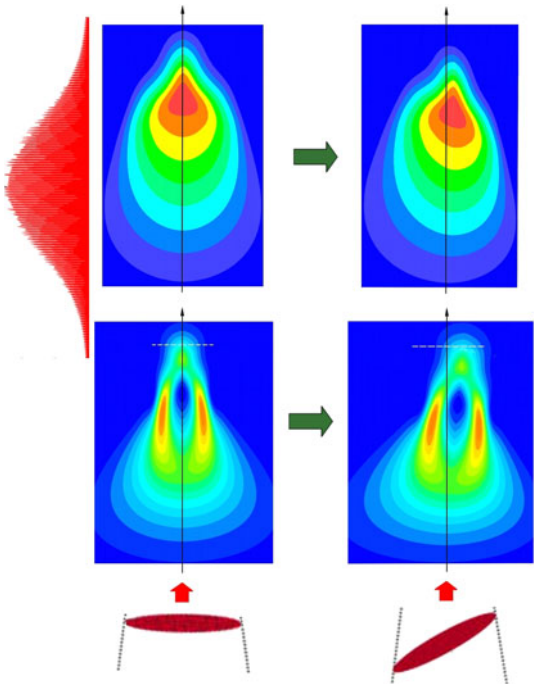

Fig. 6 Spatial distributions of the electron density (*top*) and instantaneous laser intensity (*bottom*). On the left the *maps* are calculated for the untilted Gaussian beam with 1 μJ laser energy and 150-fs pulse duration, and beam waist is 1 μm (Figs. 1a and 2a). The laser pulse propagates from the *bottom* and its temporal shape is shown for the *top left map* with zero PFT, demonstrating its spatial location with respect to the plasma structure. It is seen that the plasma is created by a small portion of energy in the pulse front. On the right imaginary pictures are given on how a nonzero PFT can distort plasma generation and beam propagation

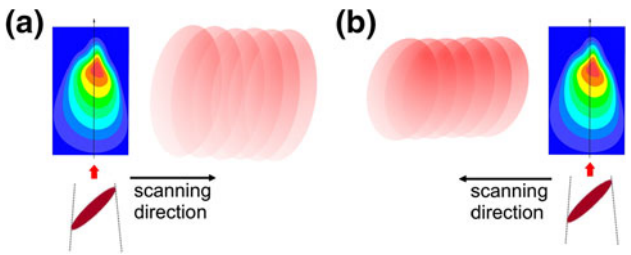

Fig. 7 Schematics for the PFT-induced laser-writing anisotropy. See text for explanations

memory resources. Alternatively, a model is under development which describes focusing of a plain laser beam ($x = r$, $y = \infty$, z). First simulation results testify our conjecture, showing that already 3° PFT induces a noticeable axial asymmetry in laser energy coupling (to be published).

6 Conclusion

We have presented the model based on Maxwell's equations supplemented with the equations of the dynamics of created electron plasma for description of the processes occurring in transparent solids in the regimes of volume modification with ultrashort laser pulses. The comparative modeling of the irradiation conditions with relatively low and high laser pulse energies has helped to understand better the excitation and thermodynamic conditions within the laser-modified region and to analyze the mechanisms responsible for the volume nanograting formation and the "quill" writing effect in glass materials observed experimentally [38]. It has been shown that for comprehensive understanding of the VNG formation, one should "marry" the LIPSS theory [65–67] with the theories of volumetric nanoplasma formation [18, 32]. This study demonstrates that laser-induced material modification is a synergetic action of laser light absorption, physics of laser-induced electron plasma, thermodynamics of laser-affected material, and mechanical material response and cannot be understood solely on the basis of nonlinear beam propagation studies. The performed analysis shows that numerical modeling is an important supplement of experimental studies and a powerful tool for understanding and predicting the underlying physics of the laser modification phenomenon. Many detailed aspects which can be overlooked in experiments due to limited resolutions of up-to-date measurement techniques may be revealed with the help of numerical simulations.

Acknowledgments The authors are grateful to P. G. Kazansky for continuous and fruitful discussions and stimulating critics, J. Bonse for valuable comments, and an undisclosed referee whose constructive remarks helped to improve the paper. This research is supported by the Marie Curie International Incoming Fellowship grant of the principal author, No. 272919, by the Russian Foundation for Basic Research (RFBR project No. 12-01-00510), and by the Ministry of Education and Science of the Russian Federation, State Contract No. 14.518.11.7021.

References

1. K.M. Davis, K. Miura, N. Sugimoto, K. Hirao, Opt. Lett. **21**, 1729 (1996)
2. R.R. Gattass, E. Mazur, Nature Photon. **2**, 219 (2008)
3. K. Miura, J. Qiu, H. Inouye, T. Mitsuyu, K. Hirao, Appl. Phys. Lett. **71**, 3329 (1997)
4. C.B. Schaffer, A. Brodeur, J.F. García, E. Mazur, Opt. Lett. **26**, 93 (2001)
5. Z. Wang, K. Sugioka, Y. Hanada, K. Midorikawa, Appl. Phys. A **88**, 699 (2007)
6. I.M. Burakov, N.M. Bulgakova, R. Stoian, A. Mermillod-Blondin, E. Audouard, A. Rosenfeld, A. Husakou, I.V. Hertel, J. Appl. Phys. **101**, 043506 (2007)
7. A. Mermillod-Blondin, I.M. Burakov, Y.P. Meshcheryakov, N.M. Bulgakova, E. Audouard, A. Rosenfeld, A. Husakou, I.V. Hertel, R. Stoian, Phys. Rev. B **77**, 104205 (2008)
8. L. Sudrie, M. Franco, B. Prade, A. Mysyrowicz, Opt. Commun. **171**, 279 (1999)
9. K. Kintaka, J. Nishii, Y. Kawamoto, A. Sakamoto, P.G. Kazansky, Opt. Lett. **27**, 1394 (2002)

10. E. Bricchi, J.D. Mills, P.G. Kazansky, B.G. Klappauf, Opt. Lett. **27**, 2200 (2002)
11. Xi. Wang, Hengchang. Guo, Hong. Yang, Hongbing. Jiang, Qihuang. Gong, Appl. Optics **43**, 4571 (2004)
12. M. Beresna, P.G. Kazansky, Opt. Lett. **35**, 1662 (2010)
13. J. Liu, Z. Zhang, S. Chang, C. Flueraru, C.P. Grover, Opt. Comm. **253**, 315 (2005)
14. A.M. Streltsov, N.F. Borrelli, Opt. Lett. **26**, 42 (2001)
15. K. Minoshima, A.M. Kowalevicz, E.P. Ippen, J.G. Fujimoto, Opt. Express **10**, 645 (2002)
16. R. Osellame, S. Taccheo, G. Cerullo, M. Marangoni, D. Polli, R. Ramponi, P. Laporta, S. De Silvestri, Electron. Lett. **38**, 964 (2002)
17. Y. Shimotsuma, M. Sakakura, K. Miura, J. Qiu, P.G. Kazansky, K. Fujita, K. Hirao, J. Nanosci. Nanotechnol. **7**, 94 (2007)
18. R. Taylor, C. Hnatovsky, E. Simova, Laser Photonics Rev. **2**, 26 (2008)
19. W.J. Cai, A.R. Libertun, R. Piestun, Opt. Express **14**, 3785 (2006)
20. A. Couairon, L. Sudrie, M. Franco, B. Prade, A. Mysyrowicz, Phys. Rev. B **71**, 125435 (2005)
21. A. Couairon, A. Mysyrowicz, Phys. Rep. **441**, 47 (2007)
22. J.R. Gulley, S.W. Winkler, W.M. Dennis, K.M. Liebig, R. Stoian, Phys. Rev. A **85**, 013808 (2012)
23. K.I. Popov, C. McElcheran, K. Briggs, S. Mack, L. Ramunno, Opt. Express **19**, 271 (2010)
24. J.R. Peñano, P. Sprangle, B. Hafizi, W. Manheimer, A. Zigler, Phys. Rev. E **72**, 036412 (2005)
25. G.M. Petrov, J. Davis, J. Phys. B: At. Mol. Opt. Phys. **41**, 025601 (2008)
26. H. Schmitz, V. Mezentsev, J. Opt. Soc. Am. B **29**, 1208 (2012)
27. D.M. Rayner, A. Naumov, P.B. Corkum, Opt. Express **13**, 3208 (2005)
28. S.M. Eaton, H. Zhang, P.R. Herman, Opt. Express **13**, 4708 (2005)
29. S. Juodkazis, K. Nishimura, S. Tanaka, H. Misawa, E.G. Gamaly, B. Luther-Davies, L. Hallo, P. Nicolai, V.T. Tikhonchuk, Phys. Rev. Lett. **96**, 166101 (2006)
30. M. Shimizu, M. Sakakura, M. Ohnishi, Y. Shimotsuma, T. Nakaya, K. Miura, K. Hirao, J. Appl. Phys. **108**, 073533 (2010)
31. M. Sakakura, T. Tochio, M. Eida, Y. Shimotsuma, S. Kanehira, M. Nishi, K. Miura, K. Hirao, Opt. Express **19**, 17780 (2011)
32. Y. Shimotsuma, P.G. Kazansky, J.R. Qiu, K. Hirao, Phys. Rev. Lett. **91**, 247405 (2003)
33. Y. Shimotsuma, K. Hirao, J.R. Qiu, P.G. Kazansky, Mod. Phys. Lett. B **19**, 225 (2005)
34. V.R. Bhardwaj, E. Simova, P.P. Rajeev, C. Hnatovsky, R.S. Taylor, D.M. Rayner, P.B. Corkum, Phys. Rev. Lett. **96**, 057404 (2006)
35. M. Hörstmann-Jungemann, J. Gottmann, M. Keggenhoff, J. Laser Micro/Nanoeng. **4**, 135 (2009)
36. K. Mishchik, G. Cheng, G. Huo, I.M. Burakov, C. Mauclair, A. Mermillod-Blondin, A. Rosenfeld, Y. Ouerdane, A. Boukenter, O. Parriaux, R. Stoian, Opt. Express **18**, 24809 (2010)
37. S. Richter, M. Heinrich, S. Döring, A. Tünnermann, S. Nolte, J. Laser Appl. **24**, 042008 (2012)
38. P.G. Kazansky, W.J. Yang, E. Bricchi, J. Bovatsek, A. Arai, Y. Shimotsuma, K. Miura, K. Hirao, Appl. Phys. Lett. **90**, 151120 (2007)
39. P. Martin, S. Guizard, P. Daguzan, G. Petite, P. D'Oliveira, P. Meynadier, M. Perdrix, Phys. Rev. B **55**, 5799 (1997)
40. D. Grojo, M. Gertsvolf, S. Lei, T. Barillot, D.M. Rayner, P.B. Corkum, Phys. Rev. B **81**, 212301 (2010)
41. Y.P. Meshcheryakov, N.M. Bulgakova, Appl. Phys. A **82**, 363 (2006)
42. M. Beresna, M. Gecevičius, P.G. Kazansky, N.M. Bulgakova, Opt. Express **19**, 18989 (2011)
43. E.G. Gamaly, A. Vailionis, V. Mizeikis, W. Yang, A.V. Rode, S. Juodkazis, High Energy Density Phys. **8**, 13 (2012)
44. R. Brückner, J. Non-Cryst. Solids **5**, 123 (1970)
45. M. Beresna, M. Gecevičius, P.G. Kazansky, Opt. Mater. Express **1**, 783 (2011)
46. M. Beresna, M. Gecevičius, P.G. Kazansky, T. Taylor, A. Kavokin, Appl. Phys. Lett. **101**, 053120 (2012)
47. J.V. Parker, J.C. Nickel, R.W. Gould, Phys. Fluids **7**, 1489 (1964)
48. R.S. Fletcher, X.L. Zhang, S.L. Rolston, Phys. Rev. Lett. **96**, 105003 (2006)
49. T.C. Killian, Nature **441**, 297 (2006)
50. C. Mézel, A. Bourgeade, L. Hallo, Phys. Plasmas **17**, 113504 (2010)
51. F. Messina, E. Vella, M. Cannas, R. Boscaino, Phys. Rev. Lett. **105**, 116401 (2010)
52. B.C. Stuart, M.D. Feit, A.M. Rubenchik, B.W. Shore, M.D. Perry, Phys. Rev. Lett. **74**, 2248 (1995)
53. V.V. Temnov, K. Sokolowski-Tinten, P. Zhou, A. El-Khamhawy, D. von der Linde, Phys. Rev. Lett. **97**, 237403 (2006)
54. M. Lenzner, F. Krausz, J. Krüger, W. Kautek, Appl. Surf. Sci. **154–155**, 11 (2000)
55. G. Petite, S. Guizard, P. Martin, F. Quéré, Phys. Rev. Lett. **83**, 5182 (1999)
56. D. Arnold, E. Cartier, D.J. DiMaria, Phys. Rev. B **45**, 1477 (1992)
57. A. Kaiser, B. Rethfeld, M. Vicanek, G. Simon, Phys. Rev. B **61**, 11437 (2000)
58. N.M. Bulgakova, R. Stoian, A. Rosenfeld, Quantum Electron. **40**, 966 (2010)
59. D.G. Papazoglow, I. Zergioti, S. Tsortzakis, Opt. Lett. **32**, 2055 (2007)
60. M. Mero, J. Liu, W. Rudolph, D. Ristau, K. Starke, Phys. Rev. B **71**, 115109 (2005)
61. V.E. Gruzdev, J.K. Chen, Appl. Phys. A **90**, 255 (2008)
62. X. Mao, S.S. Mao, R.E. Russo, G. Petite, P. Martin, Appl. Phys. Lett. **82**, 697 (2003)
63. L. Sudrie, A. Couaron, M. Franco, B. Lamouroux, B. Prade, S. Tzortzakis, A. Mysyrowicz, Phys. Rev. Lett. **89**, 186601 (2002)
64. R. Brüning, J. Non-Cryst. Solids 330, 13 (2003)
65. J.E. Sipe, J.F. Young, J.S. Preston, H.M. van Driel, Phys. Rev. B **27**, 1141 (1983)
66. J. Bonse, A. Rosenfeld, J. Krüger, J. Appl. Phys. **106**, 104910 (2009)
67. D. Dufft, A. Rosenfeld, S.K. Das, R. Grunwald, J. Bonse, J. Appl. Phys. **105**, 034908 (2009)
68. L.N. Gaier, M. Lein, M.I. Stockman, P.L. Knight, P.B. Corkum, M.Y. Ivanov, G.L. Yudin, J. Phys. B At. Mol. Opt. Phys. **37**, L57 (2004)
69. J.Z.P. Skolski, G.R.B.E. Römer, J.V. Obona, V. Ocelik, A.J. Huis in 't Veld, J.Th.M. De Hosson, Phys. Rev. B **85**, 075320 (2012)
70. D. Giulietti, G.P. Banfi, I. Deha, A. Giulietti, M. Lucchesi, L. Nocera, C.Z. Zun, Las. Part. Beams **6**, 141 (1988)
71. I.V. Khazanov, JETP Lett. **78**, 285 (2003)
72. T.Q. Jia, H.X. Chen, M. Huang, F.L. Zhao, J.R. Qiu, R.X. Li, Z.Z. Xu, X.K. He, J. Zhang, H. Kuroda, Phys. Rev. B **72**, 125429 (2005)
73. M. Sakakura, M. Terazima, Opt. Lett. **29**, 1548 (2004)
74. R.M. Waxler, G.W. Cleek, J. Res. Nat. Bur. Stand. A. Phys. Chem **77A**, 755 (1973)
75. R.A.B. Devine, Nucl. Instrum. Meth. Phys. Res. B **91**, 378 (1994)
76. E.S. Efimenko, A.V. Kim, Phys. Rev. E **84**, 036408 (2011)
77. J. Canning, M. Lancry, K. Cook, A. Weickman, F. Brisset, B. Poumellec, Opt. Mater. Express **1**, 998 (2011)
78. M. Lancry, B. Poumellec, S. Guizard, J. Laser Nano/Microengin. **7**, 217 (2012)